A panel method free-wake code for aeroelastic rotor predictions

M. Roura, A. Cuerva, A. Sanz-Andrés and A. Barrero-Gil

A panel method free-wake model to analyse the rotor flapping is presented. The aerodynamic model consists of a panel method, which takes into account the three-dimensional rotor geometry, and a free-wake model, to determine the wake shape. The main features of the model are the wake division into a near-wake sheet and a far wake represented by a single tip vortex, and the modification of the panel method formulation to take into account this particular wake description. The blades are considered rigid with a flap degree of freedom. The problem solution is approached using a relaxation method, which enforces periodic boundary conditions. Finally, several code validations against helicopter and wind turbine experimental data are performed, showing good agreement.

NOMENCLATURE

$( )'$	Integration variable
β	Blade flapping angle
β_0	Blade coning angle
β_{1c}	Longitudinal flapping angle
β_{1s}	Lateral flapping angle
Γ_b	Bound vortex strength
Γ_w	Near-wake vortex filament circulation
Γ_{tip}	Far-wake vortex filament circulation
$\mathbf{\Omega}$	Rotor angular velocity, $\Omega\mathbf{k}_O$
ν	Kinematic viscosity of air
ν_β	Non-dimensional blade rotating flap frequency
Φ	Velocity potential
Φ_{fw}	Far-wake potential
ϕ_{SHAFT}	Rotor shaft angle
ϕ_{TPP}	Tip path plane angle of attack
μ	Advance ratio, $\lvert V_\infty \rvert \cos\phi_{TPP}/(\Omega R)$
ψ	Azimuth angle measured from the x_A axis
ρ	Air density
τ	Radial wake coordinate
Θ	Auxiliary potential, $\Phi - \Phi_{fw}$
θ	Blade pitch angle
θ_0	Blade collective pitch
θ_{1c}	Lateral cyclic pitch
θ_{1s}	Longitudinal cyclic pitch
θ_{tip}	Geometric pitch at blade tip
$\Delta\Psi$	Azimuthal discretization
ξ	Wake age
a_1	Empirical constant of the viscous core
c	Blade chord
C_N	Normal aerodynamic force coefficient, $2N/(\rho(\Omega R)^2 c)$
C_T	Tangential and normal aerodynamic force coefficients, $2T/(\rho(\Omega R)^2 c)$, Rotor thrust, $T/(\rho(\Omega R)^2 \pi R^2)$
e_1	Flapping hinge offset
e_2	Root cut-out offset
I_b	Blade moment of inertia
K_v	Factor to desingularize Biot-Savart law
M	Mach number based on the blade tip speed
m	Number of panels along the blade
M_b	Weight moment
$M_{\beta a}$	Aerodynamic flapping moment
$M_{\beta g}$	Weight flapping moment
n	Number of panels around the airfoil
n_b	Number of blades
p	Pressure
R	Rotor radius
r	Non-dimensional radial distance
r_c	Vortex core radius
Re	Reynolds number based on the blade tip speed and the blade chord length
S_b	Rotor surface
S_w	Wake surface
S_{fw}	Far wake surface

S_{nw}	Near wake surface
t	Time
t^*	Time coordinate of the near wake extension
$O_A x_A y_A z_A$	Frame of reference parallel to $0_O x_O y_O z_O$, and origin 0_A in the rotor shaft
$\mathbf{0}_B x_B y_B z_B$	Frame of reference with z_B parallelto z_A, y_B parallel to blade i flap axis, and origin 0_B in the flap hinge
$\mathbf{0}_O x_O y_O z_O$	Inertial frame of reference
$\mathbf{n}_b$	Rotor surface outward unit normal vector
$\mathbf{n}_w^+$	Upper wake surface outward unit normal vector
$\mathbf{r}$	Position vector in $0_A x_A y_A z_A$
$\mathbf{V}$	Flow velocity in $0_O x_O y_O z_O$
$\mathbf{V}_b$	Blade velocity in $0_O x_O y_O z_O$
$\mathbf{V}_\infty$	Rotor translational velocity in $0_O x_O y_O z_O$, $(V_{\infty x}, V_{\infty z})$
$\mathbf{V}_{inw}$	Near wake-induced velocity
$\mathbf{V}_{te}$	Blade trailing edge velocity
HOH	Higher-order harmonics
RMS	Root mean square
NREL	National Renewable Energy Laboratory
UAE	Unsteady Aerodynamics Experiment

1. INTRODUCTION

In the present article, we focus on the rotor aeroelastic problem, i.e. the interaction between aerodynamic forces and rotor motion, due to their importance to rotor performance, vibrations and control strategies. The article is mainly devoted to the aerodynamic model, and only a simplified articulated rigid rotor mechanical model is considered.

Among the different aerodynamic theories to model the rotor aerodynamics,[1–3] vortex theories stand out as one of the most suitable approximations because of their affordable computational costs and reasonably good results. In essence, vortex models are made up of a blade aerodynamic model (lifting line, lifting surface or panel method[4]) to describe the flow around the blade and to calculate the trailed and shed vorticity released to the wake, and a prescribed[5–7] or free-wake[8–10] model to describe the wake geometry and the wake inflow.

With regard to the blade aerodynamic models, lifting line theories are widely used because of their ability to include experimental corrections to take into account different phenomena such as unsteadiness, compressibility effects or dynamic stall.[11] On the other hand, lifting surface theories and panel methods improve the blade geometry representation and are inherently unsteady. In these cases, viscous effects are included by using a viscous–inviscid interaction method,[12,13] and there have been some attempts to model separated flows by using the double-wake concept, as presented in Voutsinas.[13] Finally, as stated by Hansen *et al.*[3] and the European Wind Energy Association (EWEA),[14] boundary layer and separated flow models have not reached maturity and are still object of investigation. With reference to wake models, prescribed wake models are available for standard rotor configurations. However, free-wake models are more suitable for general rotor configurations, since the wake is allowed to freely distort under the influence of the local velocity field. The problem is that these models suffer from high computational costs, which is solved by using fast multipole methods for an efficient evaluation of the Biot–Savart law,[15–18] or by using a simplified wake model as carried out in Miller and Bliss,[8] Leishman *et al.*,[9] and Tauszig.[19]

In the present work, the wake model consists of a near vortex sheet and a far wake tip vortex filament, as presented in Figure 1. Similar near-far wake models have been used in Miller and Bliss,[8] Leishman *et al.*,[9] and Tauszig[19] for helicopter rotors. The main difference between these models and the model presented here is that they use a near wake consisting of a planar undistorted series of discrete vortices, with only trailed vorticity. In the article, the near wake is allowed to deform with the local velocity, and has taken into account trailed and shed vorticity. Finally, it is necessary to specify how to combine the far-wake model with the panel method: panel methods are based on surface integrals along the blade and the near-wake sheet. However, integration cannot be performed over the far wake because we consider it a line vortex. Its influence is incorporated into the panel method, in a similar way to when using a vortex particle wake description.[13,18,20] In these cases, the blade source intensity is modified to take into account the induced velocity of the vortex particles, or, in our case, of the tip vortices, which is determined by application of the Biot–Savart law.

For aeroelastic simulations, the aerodynamic blade-wake models presented above have to be complemented with an elastic blade model for the rotor dynamics. In this paper, a simple rigid articulated blade mechanical model, with a single flap degree of freedom, is presented.[21]

From the numerical point of view, two strategies for solving the aeroelastic problem can be implemented[9]: time-marching and relaxation methods. The former method is the more physical because the problem is solved as an initial value problem and the solution is advanced in time. This methodology is particularly suitable for purely unsteady situations such as instantaneous pitch angle variations, vortex ring or turbulent wake state, among others. However, in many situations a rotor operates under periodic conditions.[22] In these cases, it is preferable to use a relaxation approach with periodicity as a boundary condition. Relaxation methods, when possible, are preferred to time-marching methods because they are free of the numerical problems associated with the latter.[9,22] In the present work, a relaxation method has been adopted.

The paper is structured as follows. In the sections Problem Equations and Solution Process, we develop and implement the panel method free-wake methodology and the blade model. In the Results and Discussion, we validate the code against commonly agreed experimental databases: (i) the Caradonna and Tung experiments for a helicopter in hovering flight,[23] (ii) the Unsteady Aerodynamics Experiment (UAE) at the National Renewable Energy Laboratory (NREL) for the UAE wind turbine[24–26] and (iii) the articulated model rotor experiment of Harris.[27]

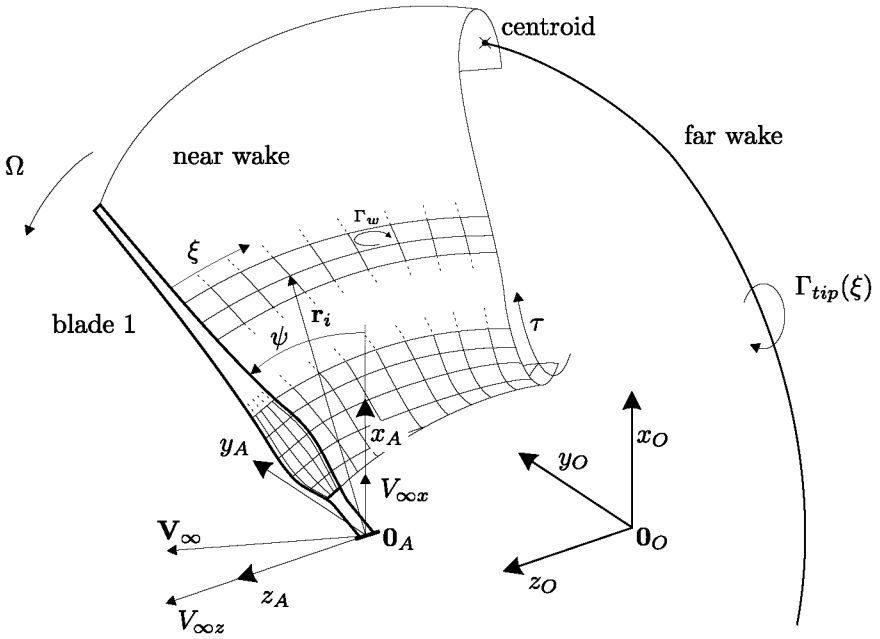

Figure 1. Implemented wake model.

2. PROBLEM EQUATIONS

Consider a n_b-bladed rotor with equal blade geometry. The blade velocity $\mathbf{V}_b$, relative to the O inertial frame of reference (Figure 1), is split into a constant translational velocity $\mathbf{V}_\infty$, and an angular velocity due to a constant rotation of value $\mathbf{\Omega}$ around the shaft, pitch angle changes $\dot{\theta}$, and blade flapping $\dot{\beta}$. The lag degree of freedom is not considered. The z_O axis has the direction of the angular velocity $\mathbf{\Omega} = \Omega\mathbf{k}_O$, and the x_Oz_O plane is oriented so that $\mathbf{V}_\infty = V_{\infty x}\mathbf{i}_O + V_{\infty z}\mathbf{k}_O$. In addition, we define a moving frame of reference A parallel to the previous frame of reference. The origin $\mathbf{0}_A$ is placed in the blade–shaft junction and moves with the rotor translational velocity $\mathbf{V}_{0_A} = \mathbf{V}_\infty$.

It is assumed that the airflow around the rotor is inviscid (high Reynolds number, $Re \gg 1$), incompressible (low Mach number, $M \ll 1$), and remains attached to the blades.

2.1. Rotor aerodynamic model

The velocity field around a rotor at high Reynolds numbers (relative to the O frame of reference) is represented as the gradient of a velocity potential $\mathbf{V} = \nabla\Phi$. The velocity potential Φ satisfies the Laplace equation $\nabla^2\Phi = 0$, with the no flux penetration boundary condition at the rotor surface $\nabla\Phi \cdot \mathbf{n}_b = \mathrm{V}_b \cdot \mathbf{n}_b$; where n_b is the rotor surface unit normal vector pointing into the fluid domain, and $\mathbf{V}_b$ the blade velocity. Far from the rotor, the air velocity tends to zero $|\mathbf{V}| \to 0$. It has been proved, using Green's third identity, that the value of a harmonic function depends on the function boundary values,[4]

$$\Phi(\mathbf{r}) = \frac{1}{4\pi}\int_{S_b}\Phi'\frac{\partial}{\partial\mathbf{n}_b'}\frac{1}{|\mathbf{r}-\mathbf{r}'|}dS_b' - \frac{1}{4\pi}\int_{S_b}\frac{\partial\Phi'}{\partial\mathbf{n}_b'}\frac{1}{|\mathbf{r}-\mathbf{r}'|}dS_b' + \frac{1}{4\pi}\int_{S_w}\Delta\Phi'\frac{\partial}{\partial\mathbf{n}_w^{+\prime}}\frac{1}{|\mathbf{r}-\mathbf{r}'|}dS_w' \quad (1)$$

where S_b is the rotor surface, S_w is the wake surface, $\Delta\Phi$ is the potential jump across the wake, and $\mathbf{n}_w^+$ is the outward unit normal vector of the upper wake surface.

In our analysis, the integral over S_w is divided into two parts in order to distinguish between the near and the far wake.[18] One integral is defined over the near-wake surface S_{nw}, which takes into account the vorticity left in the last $t * \Omega$ rotor turn, and a second integral over the far-wake surface $S_{fw} = S_w - S_{nw}$. The integral over S_{fw} defines the far-wake potential function Φ_{fw},

$$\Phi_{fw}(\mathbf{r}) = \frac{1}{4\pi}\int_{S_{fw}}\Delta\Phi'\frac{\partial}{\partial\mathbf{n}_w^{+\prime}}\frac{1}{|\mathbf{r}-\mathbf{r}'|}dS_{fw}' \quad (2)$$

Φ_{fw} satisfies Laplace's equation in the whole domain except in S_{fw}. Again applying Green's theorem to the

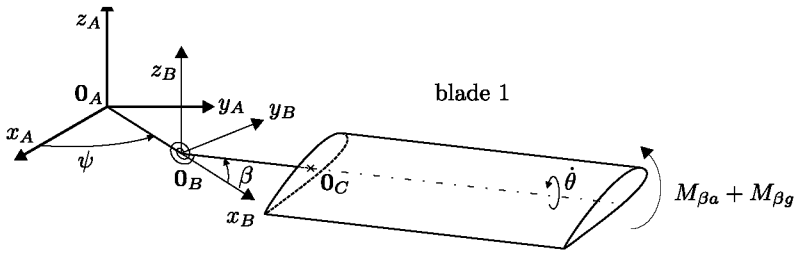

Figure 2. Rigid articulated blade model.

function Φ_{fw} over the blade's inner domain, for a point $\mathbf{r}$ in the fluid, we get[4]

$$\frac{1}{4\pi}\int_{S_b}\Phi'_{fw}\frac{\partial}{\partial\mathbf{n}'_b}\frac{1}{|\mathbf{r}-\mathbf{r}'|}dS'_b-\frac{1}{4\pi}\int_{S_b}\frac{\partial\Phi'_{fw}}{\partial\mathbf{n}'_b}\frac{1}{|\mathbf{r}-\mathbf{r}'|}dS'=0 \qquad (3)$$

Subtracting equation (3) from (1), a new integral equation for the auxiliary potential defined by $\Theta = \Phi - \Phi_{fw}$, is obtained,

$$\Theta(\mathbf{r})=\frac{1}{4\pi}\int_{S_b}\Theta\frac{\partial}{\partial\mathbf{n}'_b}\frac{1}{|\mathbf{r}-\mathbf{r}'|}dS'_b-\frac{1}{4\pi}\int_{S_b}\frac{\partial\Theta'}{\partial\mathbf{n}'_b}\frac{1}{|\mathbf{r}-\mathbf{r}'|}dS'_b+\frac{1}{4\pi}\int_{S_{nw}}\Delta\Theta'\frac{\partial}{\partial\mathbf{n}'^{+}_w}\frac{1}{|\mathbf{r}-\mathbf{r}'|}dS'_w \qquad (4)$$

where $\Delta\Theta = \Delta\Phi$, because Φ_{fw} is continuous over S_{nw}. Note that in equation (4), the S_{fw} contribution is not present. In this case, the far-wake influence appears in the boundary condition through the far-wake velocity $\nabla\Phi_{fw}$,

$$\frac{\partial\Theta}{\partial\mathbf{n}_b}=(\mathbf{V}_b-\nabla\Phi_{fw})\cdot\mathbf{n}_b \qquad (5)$$

The calculation of $\nabla\Phi_{fw}$, if a far-wake vortex sheet is considered, is computationally expensive because the Biot–Savart law has to be integrated over S_{fw}. As said in the introduction, this difficulty is overcome by replacing the far-wake vortex surface S_{fw} with a vortex filament of variable intensity Γ_{tip} (Figure 1). The main difficulty associated with this simplification is that a unique vortex filament does not define a potential flow field. Nevertheless, based on the works of Leishman,[11] and Bagai and Leishman,[28] where a similar wake geometry has been used, we assume that the vortex filament simplification gives an accurate approximation of the vortex surface far field velocity.

Finally, a relationship to couple the potential jump at the blade trailing edge with the wake potential jump is needed. This relationship is obtained by using the Kutta condition, which imposes zero pressure jump between the blade trailing edge lower surface p^-_{te}, and the blade trailing edge upper surface p^+_{te}. The development of the Kutta condition will be described in more detail in the Pressure Equation section.

A constant dipole/source singularity panel method is used to determine the auxiliary potential Θ over the blades and in the wake. The integrals over S_b and S_{nw} in equation (4) are determined by means of the formulae in the previous work.[29]

2.2. Rotor mechanical model

The blade mechanical model (Figure 2) is defined by the flapping hinge $\mathbf{0}_A\mathbf{0}_B = e_1R\mathbf{i}_B$, where R is the rotor radius, the blade root cut-out $\mathbf{0}_B\mathbf{0}_C = e_2R(cos\beta\mathbf{i}_B + sin\beta\mathbf{k}_A)$, the torsion spring at the flap hinge with spring constant k_β, the blade weight moment M_b, and the moment of inertia with respect to the y_B axis I_b. Reference frame B is defined so that z_B is parallel to z_A, y_B coincides with the flapping axis, and the origin $\mathbf{0}_B$ is in the flap hinge. The flap motion of blade 1 (Figure 2) is subjected to the aerodynamic moment $M_{\beta a}$ and the blade weight moment $M_{\beta g}$. Both are positive as β increases.

The flapping equation for the rigid articulated rotor case is obtained by using the angular momentum equation particularized for $\beta \ll 1$.[21] This blade model is coupled with the aerodynamic model presented above to determine the blade motion in aeroelastic simulations. The blade flapping equation for an articulated rotor is,

$$\frac{d^2\beta}{d\psi^2}+\nu^2_\beta\beta=\frac{M_{\beta a}+M_{\beta g}}{I_b\Omega^2} \qquad (6)$$

where ψ is the blade 1 angle measured from the x_A axis and

$$\nu^2_\beta=1+e_1R\frac{M_b}{I_b}+\frac{k_\beta}{I_b\Omega^2} \qquad (7)$$

is the non-dimensional blade rotating flap frequency.

Since the problem is considered periodic, the flapping equation (6) is solved by the Fourier–Galerkin method[30] with $\beta(\psi) = \beta_0 + \beta_{1c}cos\psi + \beta_{1s}sin\psi + HOH$, where HOH stands for higher-order harmonics.

2.3. Wake model

For a three-dimensional, inviscid and attached flow, the wake consists of a material surface with a distribution of

tangential vorticity that is released in the flow field at the blade trailing edge. The wake vorticity, for a helicopter or wind turbine, comes from two different sources: (i) trailed vorticity, which is due to the radial variation of the bound circulation, and (ii) shed vorticity, which is due to the time variation of the bound vorticity. Thanks to some visualization techniques,[5,31] it is known that the large strength of the wake trailing tip and root vortices causes the vortex sheet to roll up into two concentrated vortices, known as tip and root vortices. The hypothesis assumed here is that in the far wake the tip vortex is the dominant feature, and it is therefore possible to divide the wake into near and far vorticity. This decomposition alleviates the computation of the far wake-induced velocities, as commented in the section of the Rotor Mechanical Model. It also alleviates the wake geometry determination because only one vortex filament geometry per blade has to be computed. The wake model is depicted in Figure 1.

The time evolution of the wake geometry is governed by the motion of a set of marker points distributed along the vortex surface. The marker point locations are defined by $\mathbf{r}_i(\tau, \psi, \xi)$ (Figure 1), where the subindex $i = 1{:}\, n_b$ refers to the blade; the τ variable is the blade radial position where the marker point is created; ψ is the blade i angle measured from the x_A axis and $d\psi/dt = \Omega$; $\xi = \Omega(t - t_0)$ is the marker point age, and t_0 the time at which the marker point was first created. The marker point velocity, in the O frame of reference, is determined by using the following material surface properties: (i) a vortex sheet geometry only depends on the normal velocity (surface tangent velocities only affect the marker points distribution over the surface, but not the wake geometry), (ii) the normal velocity is continuous across the wake.[32] For these reasons, we choose the marker point velocity equal to the average of the fluid velocity on both sides of the vortex sheet, $\mathbf{V}(\mathbf{r}_i(\tau, \psi, \xi)) = \nabla(\Theta^+ + \Theta^-)/2 + \nabla\Phi_{fw}$, which has the feature that the tangential velocity induced by the local vorticity is not considered.[32] Finally, the time evolution of the wake geometry is given by

$$\frac{d\mathbf{r}_i(\tau, \psi, \xi)}{dt} = \mathbf{V}(\mathbf{r}_i(\tau, \psi, \xi)) - \mathbf{V}_\infty \tag{8}$$

The velocity $\mathbf{V}_\infty$ accounts for the A frame of reference motion.

The velocity $\mathbf{V}(\mathbf{r}_i)$ is split into two contributions, $\nabla(\Theta^+ + \Theta^-)/2$, which accounts for the blade and near wake-induced velocities $\mathbf{V}_{ib}(\mathbf{r}_i)$ and $\mathbf{V}_{inw}(\mathbf{r}_i)$, and the far-wake induction $\nabla\Phi_{fw}$ at the point $\mathbf{r}_i$. $\mathbf{V}_{ib}$ consists of the induced velocity from the distribution of sources and dipoles over the blade and is determined by means of velocity formulae developed in Hess and Smith.[29] To determine $\mathbf{V}_{inw}$, it is necessary to relate the potential jump $\Delta\Theta$ in the wake to an equivalent vorticity distribution: a constant potential wake panel is equivalent to a vortex filament ring with geometry equal to the curve bounding the panel, and intensity Γ_w, equal to the panel potential jump $\Delta\Theta$[33] (Figure 1). The velocity $\mathbf{V}_{inw}$ is then determined by means of the modified Biot–Savart law,

$$\mathbf{V}_{inw}(\mathbf{r}_i) = \int_{S_{nw}} K_v \frac{\Gamma_w}{4\pi} \frac{d\mathbf{r} \wedge (\mathbf{r}_i - \mathbf{r})}{|\mathbf{r}_i - \mathbf{r}|^3} \tag{9}$$

where the factor K_v removes the local vorticity effect,

$$K_v = \frac{h^2}{\sqrt{r_c^4 + h^4}} \tag{10}$$

h being the ortogonal distance between the direction $d\mathbf{r}$ and the point $\mathbf{r}_i$, and r_c being the vortex core dimension[34,35]

$$r_c(\xi) = 2.24\sqrt{\nu\left(1 + a_1\frac{\Gamma_w}{\nu}\right)\frac{\xi}{\Omega}} \tag{11}$$

where ν is the kinematic viscosity of air, Γ_w the wake vortex intensity, Ω the rotor angular velocity, and a_1 a model constant. It is important to note that the main influence of a_1 is on the wake geometry as wake self-induced velocities are highly dependent on its choice. For that reason, if wake geometry measurements are available, a_1 is determined by comparison between numerical and measured wake geometries. Unfortunately in some cases, wake geometry data are not available and a_1 has to be determined by other criteria, such as rotor load comparison (see The Unsteady Aerodynamics Experiment) or blade flapping comparison (see Harris' Experiment).

The far wake-induced velocities $\nabla\Phi_{fw}$ are computed by means of the Biot–Savart law,[9] in the same way $\mathbf{V}_{inw}$ is determined. The far-wake geometry is also governed by equation (8) but using a parametrization of the form $\mathbf{r}_i(\psi, \xi)$, because there is only one vortex filament per blade (τ is fixed).

Equation (8) is solved with the following initial and boundary conditions:

- As the flow over the blade is non-stalled, the wake begins at the blade trailing edge:

$$\mathbf{r}_i(\tau, \psi, 0) = \mathbf{r}_{te}(\tau, \psi) \tag{12}$$

  where $\mathbf{r}_{te}(\tau, \psi)$ is the function that gives the blade i trailing edge position.

- The far-wake tip vortex releasing point and intensity is calculated as in Bagai[36]: the tip vortex is located at the centroid of the near wake (Figure 1) and has an intensity Γ_{tip} that is related to the vorticity of the near wake's last section.
- Periodic boundary conditions are considered.[8] This point will be discussed in more detail in the section Boundary Conditions.

The free far-wake problem is numerically solved by the Bagai and Leishman pseudo-implicit technique.[28] A

two-step Adams–Moulton method is used to determine the near-wake geometry.

To complete the wake model, an equation for the time evolution of the potential jump across the wake (or wake vortex intensity) is required. This relation is obtained in in the section Pressure Equation by using the pressure continuity condition across the wake.

2.4. Boundary conditions

As said in the Introduction, a rotor operates under periodic conditions in several situations. In these cases, an entire rotor revolution has to be solved to determine the problem solution at any time. However, if some assumptions are made, as there is equal blade geometry and equal blade motion at each azimuth angle ψ, the problem solution at ψ is blade independent and only $1/n_b$ rotor revolution has to be solved.[8] These simplifications lead to a different boundary condition to the classical periodicity $f(\psi) = f(\psi + 2\pi)$. The particular boundary conditions used in the aerodynamic and the aeroelastic problems are as follows:

- Aerodynamic problem: the blade motion is totally specified. The pitch–flap law is unique for all blades $\zeta(\psi) = \zeta_0 + \sum_{n=1}^{\infty} \zeta_{nc}\cos(n\psi) + \zeta_{ns}\sin(n\psi)$, where $\zeta = (\theta, \beta)$ are the pitch and flap angles. We look for solutions that fulfil the general periodicity condition $\boldsymbol{\delta}_i(\psi) = \boldsymbol{\delta}_i(\psi + 2\pi)$, where $\boldsymbol{\delta}_i(\psi)$ is the problem solution associated with blade $i = 1$: n_b for the azimuthal position ψ. However, we can take advantage of the blade geometry equality and the unique pitch–flap law and look for solutions that fulfil the particular periodicity condition $\boldsymbol{\delta}_{i+1}(\psi) = \boldsymbol{\delta}_i(\psi)$($i + 1$ represents the blade after blade i; the blade after blade n_b is 1). For a two-bladed rotor, this condition leads to $\boldsymbol{\delta}_1(0°) = \boldsymbol{\delta}_2(0°)$ and $\boldsymbol{\delta}_2(180°) = \boldsymbol{\delta}_1(180°)$. This means that for a two-bladed rotor, only 180° have to be solved, i.e. the solution for blade 1 has to be determined when $\psi \in [0°, 180°]$ and for blade 2 when $\psi \in [180°, 360°]$ (observe that geometrically $\psi = 0°$ is the same as $\psi = 360°$). In the following 180° necessary to solve a whole rotor turn, the solution is exchanged, i.e. the solution for blade 1 when $\psi \in [180°, 360°]$ is the same as the solution for blade 2 when $\psi \in [180°, 360°]$. This is similarly carried out for the solution for blade 2.
- Aeroelastic problem: the blade motion depends on the aerodynamic loads, and the fluid–structure interaction has to be analysed. The case of an articulated rigid rotor with a given pitch law and undetermined flap motion is equivalent to the aerodynamic problem if a flap law of the form $\beta(\psi) = \beta_0 + \beta_{1c}cos\psi + \beta_{1s}sin\psi$ is prescribed; $(\beta_0, \beta_{1c}, \beta_{1s})$ have to fulfil the flap dynamic equation (6). In our analysis, higher-order harmonics are considered negligible.

2.5. Pressure equation

The present section contains two parts. The first part deals with the modification of the Bernoulli equation for the pressure calculation. In the second part, the relations for the Kutta condition and for the time evolution of the wake potential jump (wake vorticity intensity) are presented.

Pressure is computed by means of the unsteady Bernoulli equation, with potential $\Phi = \Theta + \Phi_{fw}$, velocity $\mathbf{V} = \nabla(\Theta + \Phi_{fw})$, velocity–pressure conditions at infinity $(\mathbf{V}, p)|_\infty = (\mathbf{0}, p_\infty)$ and gravity forces negligible.

$$\frac{\partial(\Theta + \Phi_{fw})}{\partial t} + \frac{|\nabla(\Theta + \Phi_{fw})|^2}{2} = -\frac{p - p_\infty}{\rho} \tag{13}$$

Note that the potential time derivative is defined in the O inertial frame of reference and therefore, for a point 's' at the domain boundary, with potential Φ and velocity $\mathbf{V}_s$ with respect to the O reference frame, the unsteady term ∂_t in equation (13) is determined by using the following relationship:

$$\frac{\partial(\Theta + \Phi_{fw})}{\partial t} = \left.\frac{d(\Theta + \Phi_{fw})}{dt}\right|_s - \mathbf{V}_s \cdot \nabla(\Theta + \Phi_{fw}) \tag{14}$$

where $d_t|_s$ is the temporal derivative following the point 's'. Substituting (14) into (13) we obtain

$$\left.\frac{d(\Theta + \Phi_{fw})}{dt}\right|_s + \left(\frac{\nabla(\Theta - \Phi_{fw})}{2} - \mathbf{V}_s\right) \cdot \nabla(\Theta + \Phi_{fw}) = -\frac{p - p_\infty}{\rho} \tag{15}$$

which is the equation used for the pressure calculation. Pressure forces are calculated by pressure integration over the blade surfaces. The far wake potential Φ_{fw} is determined by integrating the velocities $\nabla\Phi_{fw}$ over the blade. This integral should depend only on the endpoints, but here, as the value of $\nabla\Phi_{fw}$ is approximated by the velocity due to the tip vortices, there are slight differences depending on the integration path.

At this point, it is of interest to estimate the order of magnitude of the pressure jump between the lower and the upper side of an airfoil. Let us consider an airfoil situated at a distance r from the rotor shaft, with chord c, angular velocity Ω and bound circulation Γ_b. Then $d_t(\Theta + \Phi_{fw}) \sim \Gamma_b/t_c$ ($t_c \sim 1/\Omega$ is the characteristic time scale), $\nabla(\Theta + \Phi_{fw})/2 - \mathbf{V}_s \sim \Omega r$, $\nabla(\Theta + \Phi_{fw}) \sim \Gamma_b/c$, and therefore the pressure order of magnitude is $\Delta p_c/\rho \sim \Gamma_b\Omega(1 + r/c)$. For typical blade aspect ratios, the contribution of the unsteady term is negligible compared to the circulatory term because $c/r \ll 1$. Only when $r/c \sim 1$ (blade root) are unsteady and circulatory terms of the same order. The airfoil pressure jump is

$$\frac{\Delta p_c}{\rho} \sim \frac{\Gamma_b \Omega r}{c} \tag{16}$$

Let us now attempt to determine a relationship for the Kutta condition and the time evolution of the wake potential jump. To achieve this, it is necessary to calculate the pressure difference for a point 's' situated just over (+) and below (−) the blade trailing edge and the wake sheet, respectively, and impose zero pressure jump,

$$\left.\frac{d(\Theta^+ - \Theta^-)}{dt}\right|_s + \left(\frac{\nabla(\Theta^+ + \Theta^-)}{2} + \nabla\Phi_{fw} - \mathbf{V}_s\right)\cdot \nabla(\Theta^+ - \Theta^-) = -\frac{p_s^+ - p_s^-}{\rho} = 0 \tag{17}$$

herein, the relations $\Phi_{fw}^{\pm} = \Phi_{fw}$ and $\nabla\Phi_{fw}^{\pm} = \nabla\Phi_{fw}$ have been used.

- For the Kutta condition case equation (17) is particularized for the blade trailing edge, $\mathbf{V}_s = \mathbf{V}_{te}$, and the condition of zero pressure jump is substituted by the condition of blade trailing edge pressure jump much smaller than the airfoil pressure jump order of magnitude $(p_{te}^+ - p_{te}^-)/\rho \ll \Gamma_b \Omega r/c$

$$\left.\frac{d(\Theta^+ - \Theta^-)}{dt}\right|_{te} + \left(\frac{\nabla(\Theta^+ + \Theta^-)}{2} + \nabla\Phi_{fw} - \mathbf{V}_{te}\right)\cdot \nabla(\Theta^+ - \Theta^-) \ll \frac{\Gamma_b \Omega r}{c} \tag{18}$$

In equation (18), the order of magnitude of the unsteady term is the same as in equation (15) and thus negligible compared to $\Gamma_b \Omega R/c$. For this reason, equation (18) is substituted by

$$\left(\frac{\nabla(\Theta^+ + \Theta^-)}{2} + \nabla\Phi_{fw} - \mathbf{V}_{te}\right)\cdot \nabla(\Theta^+ - \Theta^-) = 0 \tag{19}$$

where $(\nabla(\Theta^+ + \Theta^-)/2 + \nabla\Phi_{fw} - \mathbf{V}_{te})$ is the marker point velocity for an observer at the trailing edge. Equation (19) indicates that the potential jump derivative at the blade trailing edge $\xi = 0$, in the $\tau = \tau_0$ direction, is zero (Figure 3).

- The point 's' is a wake marker point. In this case, the velocity is $\mathbf{V}_s = \nabla(\Theta^+ - \Theta^-)/2 + \nabla\Phi_{fw}$; replacing $\mathbf{V}_s$ into equation (17), we obtain

$$\left.\frac{d(\Theta^+ - \Theta^-)}{dt}\right|_s = 0 \tag{20}$$

which indicates that the wake potential jump following a marker point remains constant in time.

3. SOLUTION PROCESS

In this section, we consider the resolution process of the aerodynamic and aeroelastic problems presented in the section Boundary Conditions.

3.1. Aerodynamic problem

The first case study presented here deals with the resolution process of the aerodynamic problem (Figure 4). Given an initial wake geometry that fulfil the particular boundary conditions, the rotor aerodynamics is solved by means of the panel method formulation. Next, the near–far-wake geometry is updated and a new iteration is begun. The solution is converged when the root mean square (*RMS*) of the distance moved by the far-wake marker points between two iterations is less than a specified threshold ε.

3.2. Aeroelastic problem

This second case deals with the aeroelastic problem resolution. The problem consists of a set of n unknown variables and n conditions to fulfil. As an example, for an

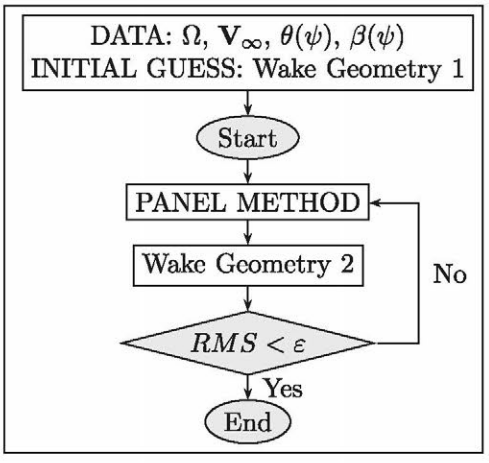

Figure 4. Aerodynamic problem resolution layout.

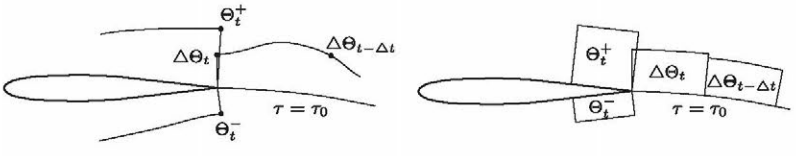

Figure 3. Profile Kutta condition in continuous and discretized form; $\Delta\Theta_t = \Delta\Theta(t) = \Theta^+(t) - \Theta^-(t) = \Theta_t^+ - \Theta_t^-$.

articulated rotor with a given pitch law and an undetermined flapping law, the unknown variables are the flapping law coefficients (β_0, β_{1c}, β_{1s}), and the conditions consist of the errors in the harmonic projections of equation (6).

The problem solution procedure is as follows (Figure 5): given an initial condition for the velocity field (which defines a periodic wake geometry in the sense of the particular boundary conditions), a non-linear system of equations solver is used to determine the control variables from the different harmonic projections of the flapping equation. Next, the velocity field is updated, a new wake geometry is obtained, and a new solver iteration is begun. The aeroelastic problem is solved when the far-wake geometry variation between two iterations is less than a given error $RMS < \varepsilon$. Note that during the non-linear solver process of resolution the wake velocity field is not updated. Updating the velocity field leads to convergence errors because the same target values of the unknown variables, in two distinct iterations, lead to distinct errors in the system of equations because of changes in the wake geometry. However, the wake geometry is calculated in every non-linear solver iteration so that it has to start at the blade trailing edge.

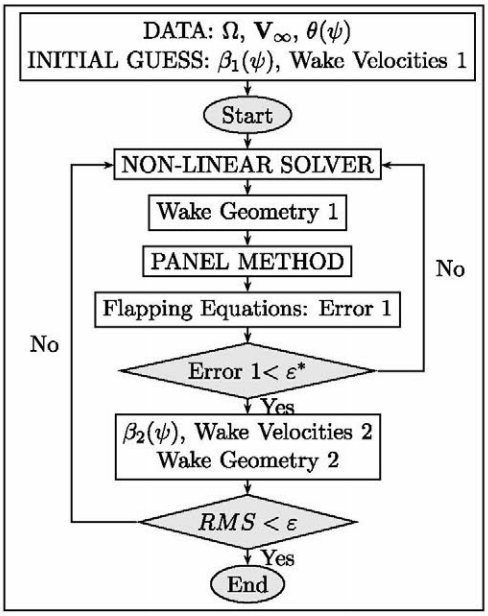

Figure 5. Aeroelastic problem resolution layout.

4. RESULTS AND DISCUSSION

4.1. The caradonna–tung experiment

The Caradonna–Tung experiment (CT) was performed on a helicopter rotor model with constant chord, untwisted blades and NACA 0012 airfoils in hovering flight.[23] The operational conditions considered in this section are $\Omega R = 150\ \mathrm{m\ s^{-1}}$ and collective pitch of $\theta_0 = 12°$. The base simulation uses the following numerical parameters $a_1 = 0.1$, $(m, n) = (30, 74)$, near-wake extension $t * \Omega = 250°$, $\Delta\psi = 5°$, and total wake extension of 11.8 turns.

Figure 6 compares the tip vortex geometry between measurements and simulations for different values of a_1. As it is seen in Figure 6(b), the best agreement between simulation and experimental results is obtained for $a_1 = 0.1$. It is important to stand out the differences between the values of $a_1 \in [10^{-4}, 10^{-5}]$ recommended in Ananthan *et al.*,[34] and Ramasamy and Leishman,[35] and the value of $a_1 = 0.1$ determined. However, this value is equal to the one found in Bagai.[36] Additionally, similar to Bagai,[36] for values of a_1 smaller than 0.1, the problem exhibits poor convergence because of the high mutual influence between vortex filaments. In our case, it is found that simulations with $a_1 < 0.07$ do not converge.

Figures 7 and 8 show the experimental and numerical spanwise distribution of the normal and tangential aerodynamic force coefficient $C_{N,T} = 2(N, T)/(\rho(\Omega R)^2 c)$, for dif-

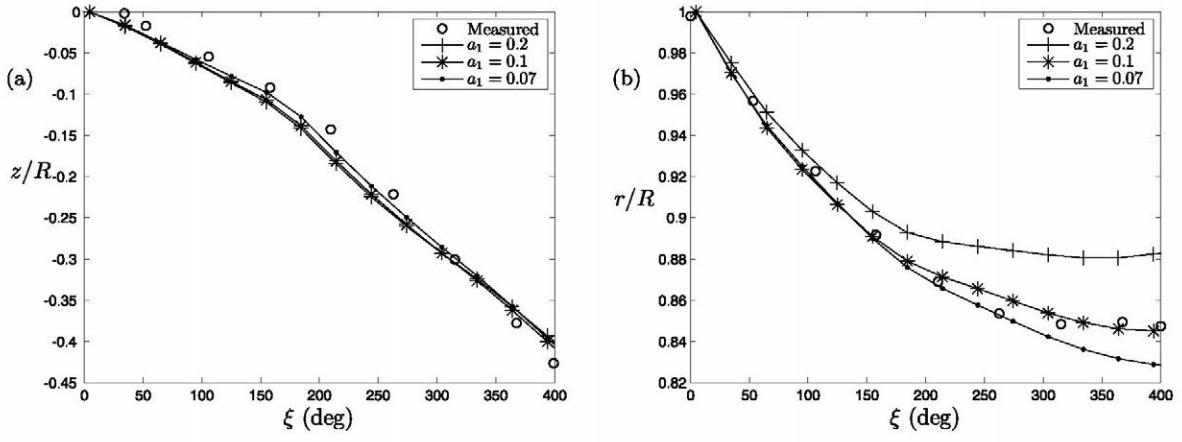

Figure 6. Comparison between measured and computed tip vortex geometry (a) z_A-coordinate and (b) radius or wake contraction for different values of a_1.

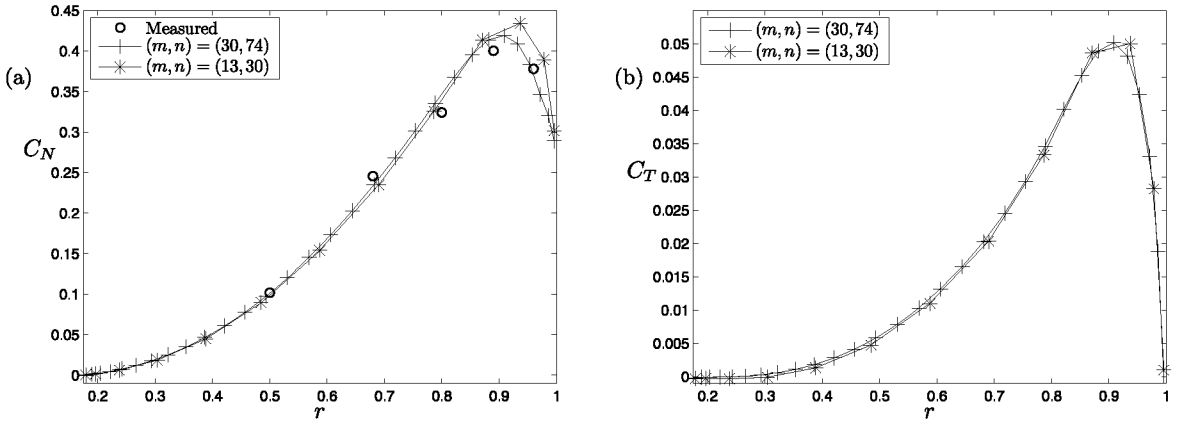

Figure 7. Spanwise distribution of (a) normal C_N and (b) tangential C_T force coefficients for different blade discretizations (m, n).

ferent values of blade discretization and near-wake extensions, respectively. C_N and C_T represent the dimensionless aerodynamic forces acting perpendicular and parallel to the airfoil chord. In Figure 7, computations have been performed with two different blade discretizations (m, n), where m is the number of panels in the spanwise direction, and n is the number of panels around the airfoil. As can be seen, force distributions do not change appreciably. Only C_N is overpredicted at the blade tip for the coarse discretization. In Figure 8, the force coefficient computations have been performed with different near-wake extensions $t * \Omega = [250°, 175°, 50°]$, while the total wake extension is kept constant at 11.8 turns: from simulations it is observed that the last near wakes extend a distance of 0.26, 0.19, and 0.07 rotor diameters downstream, and the whole wake is kept constant at 2.1 rotor diameters downstream. It is also presented, in dashed line form, computations without considering the far-wake tip vortex influence. $C_{N,T}$ without the far wake are calculated as in Figure 4, adding an extra iteration, when the problem is converged, with the far wake influence omitted, $\nabla\Phi_{fw} \cdot \mathbf{n}_b = 0$ in equation (5). It is important to note the coincidence between the different $C_{N,T}$ distributions with the far-wake influence corresponding to different near wakes $t * \Omega$. The equivalence is higher at the blade tip, whereas at the blade root, there are small differences because the root-trailed vorticity has been removed in the far wake. This fact confirms our hypothesis that the far wake tip vortex is an accurate representation of the far vortex surface in hovering flight.

4.2. The unsteady aerodynamics experiment

The UAE is divided into six campaigns. Here we only use data from the NREL Phase IV[24] and Phase VI[37] campaigns. These campaigns correspond to a three-/two-bladed, non-tapered/tapered wind turbine, both using twisted blades with S809 airfoils. The NREL Phase IV experiment was performed in field conditions and therefore presents large temporal and spatial variations in the incident air speed vector. For comparisons, a preliminary data selection is necessary to remove the cases with high velocity fluctuations, in order to minimize data variability (shear, turbulence, and other in field non-desired effects cannot be removed). The NREL Phase VI experiment was conducted in the NASA Ames Research Center wind tunnel to remove, or at least have some control, over all previous NREL experiments uncertainties. This section is concerned about yawed NREL rotor working conditions. From a numerical point of view, it is important to indicate that only the blade geometry from the maximum chord on is modelled.

For clarity, as now fluid variables are time dependent, code sensitivity to numerical parameters [a_1, (m, n), $t * \Omega$, $\Delta\psi$], and comparisons between experimental data and computations are depicted in different figures. Table 1 lists the operational conditions of the figures in this section, and Table 2 lists the computational parameters used in each case.

As said in the section of the Wake Model, in the case that no wake geometry data are available, a_1 should be determined by comparison with experimentally measured loads. Unfortunately, the wind turbine wake geometry is fundamentally governed by $\mathbf{V}_\infty$, and the effect of self-induced velocities is low compared to $\mathbf{V}_\infty$. For that reason, the influence of a_1 on rotor loads is almost not appreciable, as seen in Figure 9, and cannot be determined by rotor load comparison. However, for similarity to the CT case and for wake convergence reasons, a_1 is chosen equal to 0.1. Therefore, in the case of a wind turbine rotor, wake geometry measurements are crucial to determining a_1. In connection with this, the recent MEXICO project[38] incorporates particle image velocimetry (PIV) measurements that allow the determination of the tip vortex trajectories. These trajectories can be used to accurately determine a_1.

Figure 10 shows the $C_{N,T}$ sensitivity to blade discretization (m, n). No appreciable variation is observed. In a similar way, Figure 11 shows the $C_{N,T}$ coefficient

sensitivity to the near-wake extension $t * \Omega$, while the total wake extension is kept constant. In this case, the aerodynamic force coefficients present some sensitivity to the wake extension, meaning that in the case of yawed conditions the tip vortex approximation is a worse approximation than in axial conditions. It is a well-known fact that the influence of the root vortex is important in yawed configurations,[39] and for accurate simulations its influence has to be modelled. The idea here is to extend as much as possible the general near wake to keep the influence of the root vortex, which is not considered in our far wake model. As a rule of thumb, the minimum near-wake extension should be chosen so it is higher than the azimuthal distance between two blades. Also, computations using different azimuthal discretizations, $\Delta\psi = 5°$, $\Delta\psi = 8°$ and $\Delta\psi = 10°$, have been performed, without appreciable differences between them.

Finally, from the experimental validation point of view, two cases are presented. Figures 12 and 13 show the experimental and numerical force coefficients during a blade

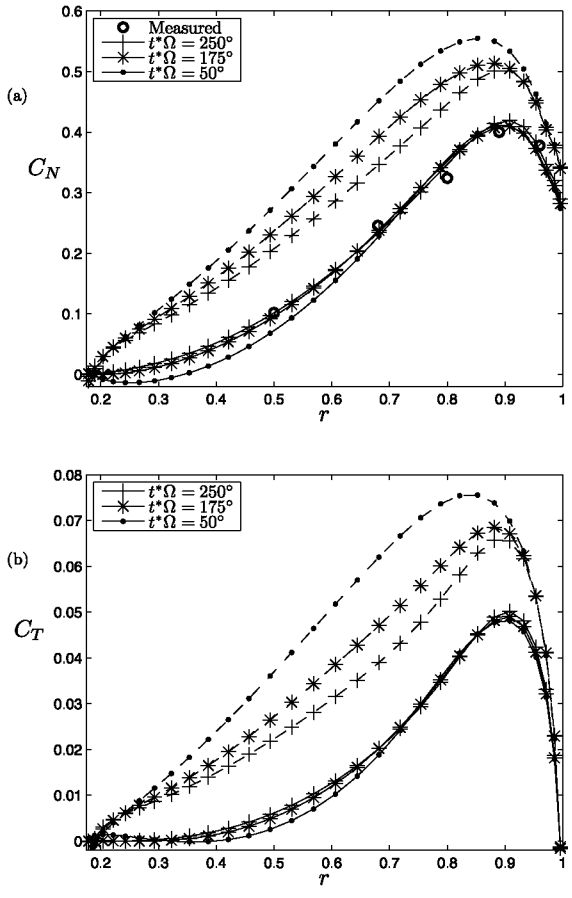

Figure 8. Spanwise distribution of (a) normal C_N and (b) tangential C_T force coefficients when varying the near-wake extension $t \times \Omega$. Dashed curves mean simulations computed without the far wake influence.

Table 2. Computational parameters for the section's figures.

Figure	a_1	(m,n)	$t * \Omega$ (deg)	$\Delta\psi$ (deg)	Total wake extension (turns)
9	—	(20,50)	450	5	12.4
10	0.1	—	175	5	6.1
11	0.1	(25,60)	—	5	6.1
12	0.1	(20,50)	450	5	12.4
13	0.1	(20,50)	360	6	9.3

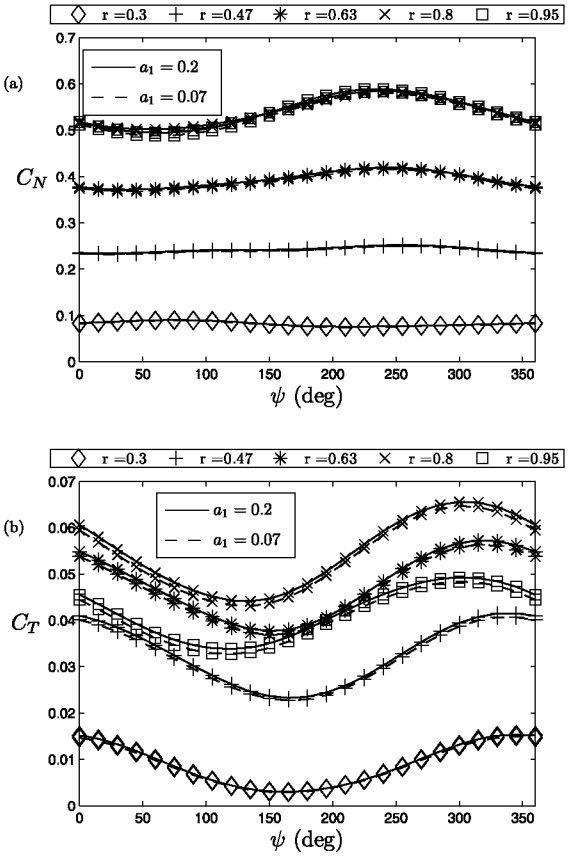

Figure 9. Influence of the viscous constant a_1 on the azimuthal variation of the (a) normal C_N and (b) tangential C_T force coefficients at different blade radial stations.

Table 1. Operational conditions for the section's figures.

Figure	NREL Phase	ρ (kg m^{-3})	$\lvert \boldsymbol{V}_\infty \rvert$ (m s^{-1})	Yaw (deg)	Ω (rpm)	Tip speed ratio	θ_{tip} (deg)	β_0 (deg)
9, 12	VI	1.234	7.1	20.0	71.9	5.4	3.0	3.4
10	IV	0.965	7.1	42.2	71.6	5.3	2.8	3.4
11	IV	0.963	9.8	21.0	72.2	3.9	2.9	3.4
13	IV	0.963	10.8	42.4	72.0	3.5	2.9	3.4

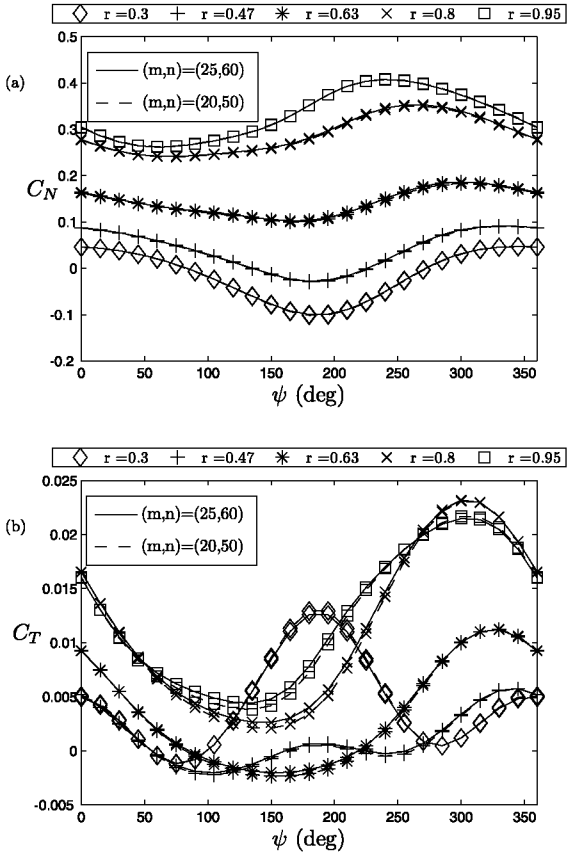

Figure 10. Influence of the blade discretization (*m*, *n*) on the azimuthal variation of the (a) normal C_N and (b) tangential C_T force coefficients at different blade radial stations.

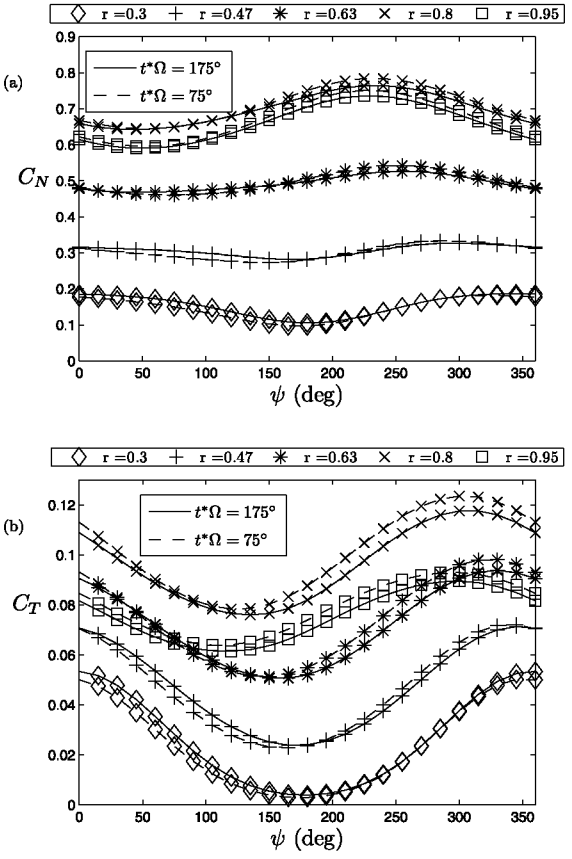

Figure 11. Influence of the near-wake extension $t^* \Omega$ on the azimuthal variation of the (a) normal C_N and (b) tangential C_T force coefficients at different blade radial stations.

turn at different radial stations. As seen in Table 2, the near-wake extension used in each case has 450° and 360°. These near-wake extensions correspond to a maximum distance, measured from the rotor plane in the direction of the wind velocity $\mathbf{V}_\infty$, of 0.72 and 0.98 rotor diameters, respectively. Good agreement between the experimental and numerical results is found except at $\psi \sim 180°$ in Figure 12 and at $\psi \sim 150°$ in Figure 13, where experimental data are perturbed by the tower shadow,[40] and in Figure 13(b) where C_T experimental values at radial stations r = [0.3, 0.63], around $\psi \sim 0°$, 360°, present a large decay due to stall effects.[21,41] Both effects are out of the scope of this paper because the model does not take them into account.

4.3. Harris' experiment

Harris' experiment was performed on a tandem model helicopter with the fore rotor removed. The rotor is four bladed, twisted, with no tapper and V23010-1.58 airfoils.[27] The experiment consists of determining the blade flapping response (β_0, β_{1c}, β_{1s}), the shaft angle ϕ_{SHAFT} and the collective pitch angle θ_0, subjected to the conditions of tip path plane angle of attack $\phi_{TPP} \simeq 1°$, thrust coefficient $C_T \simeq 7.1 \cdot 10^{-3}$ and articulated blade model for the blades motion, given the values of the cyclic pitch controls (θ_{1c}, θ_{1s}) = (0°, 0.73°) and the advance ratio $\mu = |\mathbf{V}_\infty| cos\varphi_{TPP}/(\Omega R)$. Observe that the experiment corresponds to an aeroelastic problem where ϕ_{SHAFT} and θ_0 have been added to the unknown variables and ϕ_{TPP} and C_T to the conditions to fulfil. Also note that the fuselage is not removed; thus, experimental data include aerodynamic fuselage effects.

The major difficulty in simulating Harris' experiments has to do with the negative tip path plane angle of attack, which favours the occurrence of blade vortex interactions (BVI).[2] BVI produces a loss of accuracy in the far-wake vortex geometry. In our case, for $\mu = 0.05$ on $RMS \in$ [0.03, 0.001]; for $\mu < 0.05$, convergence is recovered again $RMS < 0.001$, due to higher inflow at low advance ratios, which rapidly convects the wake vortices downstream far from the blades. Figure 14(a) shows the typical *RMS* convergence for high and low advance ratios. As commented above, the desired convergence is not reached for high advance ratios. In order to obtain a major insight into the *RMS* convergence, in Figure 14(b) the L^2-norm of the

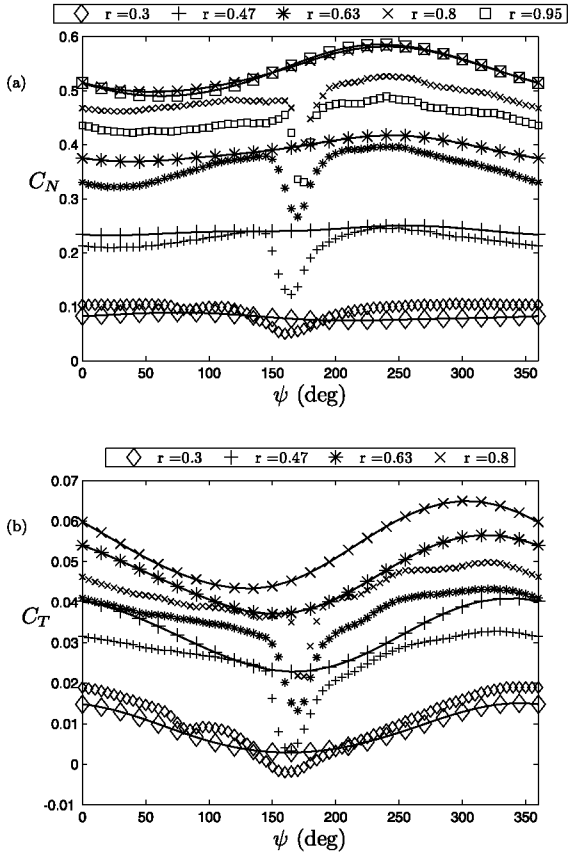

Figure 12. Experimental (small markers) and numerical (markers with solid line) azimuthal variation of the (a) normal C_N and (b) tangential C_T force coefficients at different blade radial stations. For clarity in (b) only four radial stations are presented.

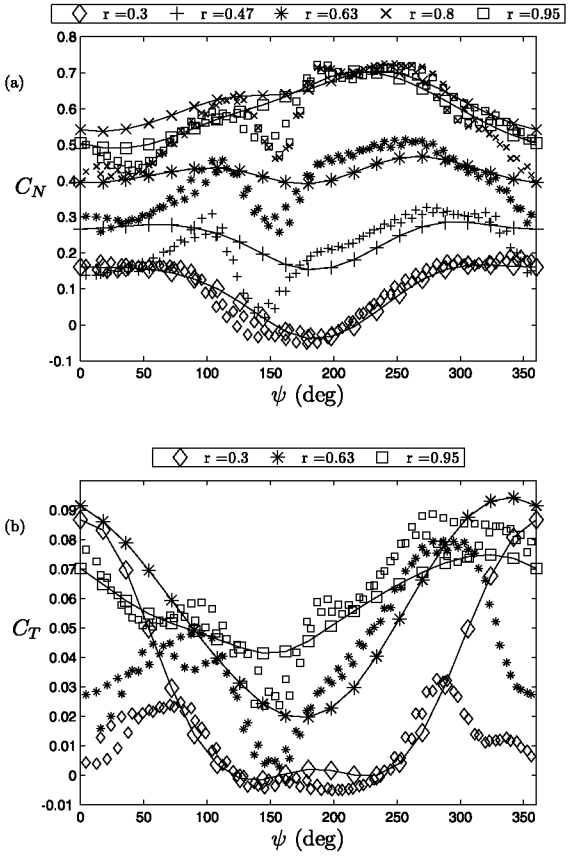

Figure 13. Experimental (small markers) and numerical (markers with solid line) azimuthal variation of the (a) normal C_N and (b) tangential C_T force coefficients at different blade radial stations. For clarity in (b), only three radial stations are presented.

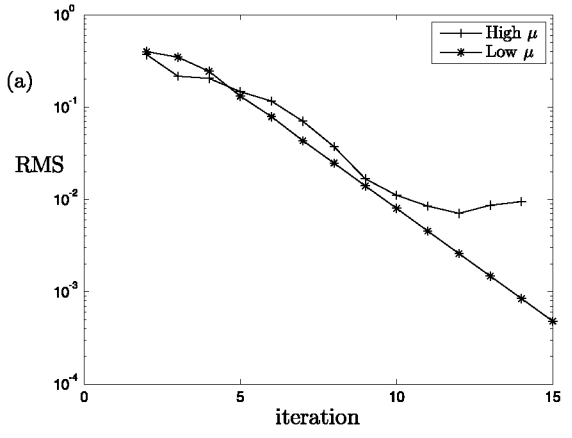

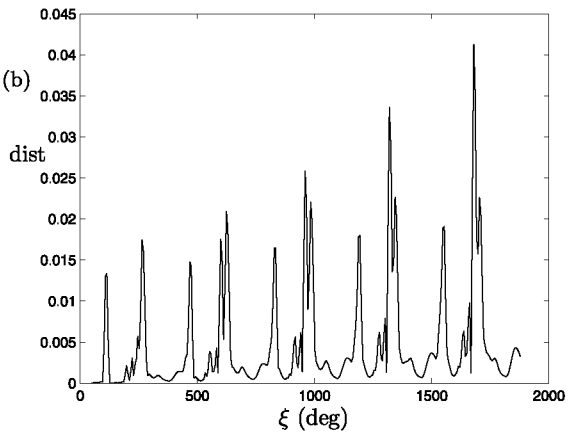

Figure 14. (a) Typical RMS convergence trend. (b) Typical distance variation in the far wake control points between two wake geometry iterations. Peaks correspond to BVI.

position variation of the far-wake control points between two iterations is presented as a function of the wake age ξ. Observe that the maximums in the L^2-norm occur at $\zeta = [90°, 270°, 450°, \ldots, 1530°, 1710°]$: the explanation of the sequence is that when $\zeta = 90°$ and $\zeta = 270°$ the peak in distance is due to the BVI, for $\zeta \geq 450°$ the peaks correspond to the previous BVI when $\zeta = [90°, 270°]$ that have been convected downstream. Related to the BVI is the elec-

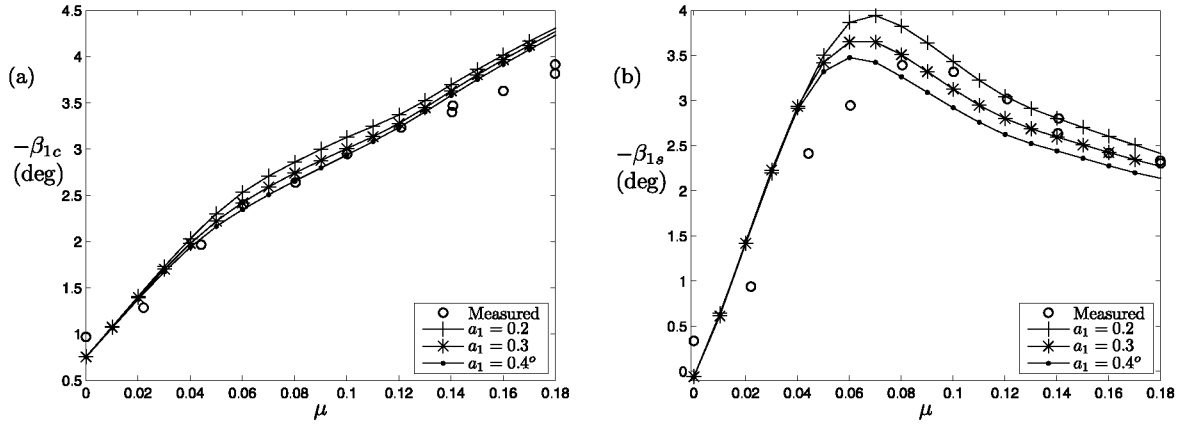

Figure 15. Comparison between measured and simulated (β_{1c}, β_{1s}) curves as a function of the advance ratio μ.

tion of the near-wake extension. If too long, the wake intersects the preceding blade and the program crashes. To avoid this situation, the near-wake extension should be less than the distance between blades $t * \Omega < \pi/2$ (exception to the rule of thumb presented in the section The Unsteady Aerodynamics Experiment).

However, despite all the drawbacks presented above, simulation results are in good agreement with experimental data. Figures 15(a), (b) show the numerical and experimental curves of β_{1c} and β_{1s} as a function of the helicopter advance ratio. The simulations are performed with the following computational parameters: $(m, n) = (16, 38)$, near-wake extension $t * \Omega = 48°$, azimuthal discretization $\Delta\psi = 6°$, total wake extension 5.5 turns, and different three different values of a_1 = [0.1, 0.2, 0.3]. The major differences in β_{1s} are at low advance ratios until the β_{1s} peak value, due to the high slope of the numerical curves. One possible explanation of these differences is the presence of the fuselage in the experiments. On the other hand, good agreement between experimental and numerical simulations is observed in the whole μ range for β_{1c}. The best experimental to simulation agreement is for $a_1 = 0.3$. Especially important for the code validation is to reproduce the main β_{1s} curve features because it is known to be highly dependent of the wake inflow.[42] Whereas $\beta_{1c}(\mu)$ is easily obtained with a simple Blade Element Momentum (BEM) model with uniform inflow.

5. CONCLUSIONS

A panel method free-wake code has been developed and validated. The main code characteristics are the wake simplification into near and far wake, and the particular periodic boundary conditions used. Both simplifications make the code run faster and this leads to an important reduction in computational requirements. All computations have been performed on a quad-core, 2GB RAM, 3 GHz personal computer. From the validation point of view, it can be seen that despite such simplifications, the numerical results are in good agreement with experimental data, confirming the validity of the hypotheses used. However, the code presents one major drawback: only an inviscid, incompressible and attached flow can be studied. A further goal would be to combine the code with a boundary layer theory and the implementation of the exact non-linear Kutta condition.

ACKNOWLEDGEMENT

This work was supported by the Spanish Ministry of Education and Science in the framework of the project 'Modelos del comportamiento dinámico de parques eólicos- CGL200506966-C07-06'.